PAPER

The plasma morphology of an asymmetric electrode ablative pulsed plasma thruster

View the article online for updates and enhancements.

IOP ebooks™

Bringing you innovative digital publishing with leading voices to create your essential collection of books in STEM research.

Start exploring the collection - download the first chapter of every title for free.

The plasma morphology of an asymmetric electrode ablative pulsed plasma thruster

Zhe Zhang[1]**, William Yeong Liang Ling**[2] **, Junxue Ren**[3]**, Haibin Tang**[4] **, Jinbin Cao**[4]**, Xin Lin**[5] **and Thomas M York**[6]

[1] School of Instrumentation and Optoelectronic Engineering, Beihang University, Beijing 100191, People's Republic of China
[2] School of Aerospace Engineering, Beijing Institute of Technology, Beijing 100081, People's Republic of China
[3] School of Astronautics, Beihang University, Beijing 100191, People's Republic of China
[4] School of Space and Environment, Beihang University, Beijing 100191, People's Republic of China
[5] Institute of Mechanics, Chinese Academy of Sciences, Beijing 100080, People's Republic of China
[6] Professor Emeritus, Ohio State University, Columbus, Ohio 43235, United States of America

E-mail: thb@buaa.edu.cn

CrossMark

Abstract

The ablative pulsed plasma thruster (APPT) is a typical form of electric propulsion that is highly suitable for micro-satellites. However, its low performance has been a main drawback. Recently, an asymmetric segmented anode schematic was shown to enhance the performance of APPTs. The improved thrust performance obtained with the use of a segmented anode can potentially enable promising applications in future space tasks. To further understand the physical processes behind a segmented anode APPT, experiments using an ultra-high-speed camera, narrow bandpass filters, and a magnetic probe were conducted with both normal parallel-plate electrodes and a segmented anode on an experimental APPT. Successive images of light emission from C^+, neutral C_2, and broadband emission reveal the evolution of the plasma morphology on an APPT with a segmented anode. The magnetic field strength profiles show that the inter-electrode plasma propagation velocity of a segmented anode APPT is approximately $19 \, \mathrm{km \, s^{-1}}$, which is slightly lower than that of a normal APPT at $23 \, \mathrm{km \, s^{-1}}$. However, the similar order of magnitude suggests a similar downstream acceleration mechanism between the two. The arc morphology observed in the high-speed images shows that the segmented anode APPT with asymmetric electrodes has a restricted arc attachment point, possibly resulting in stronger arc current density at the anode corner. This should result in higher ionization and ablation when compared with a normal anode APPT. Based on the results here, we hypothesize that the segmented anode APPT may be able to better utilize the restrike energy in the propellant ionization process. This fundamentally changes the physical process behind APPT operation, meaning that the improvements should also be applicable to other APPT designs. It can also be adopted as an additional step in the overall optimization of an APPT design.

Supplementary material for this article is available online

Keywords: ablative pulsed plasma thruster, segmented anode, ultra-high-speed camera, arc morphology

1. Introduction

Electric propulsion (EP) systems are space propulsion systems with the advantage of a high fuel efficiency, making them attractive in spacecraft orbital control. Recently, an increasing number of satellites have adopted EP for spacecraft orientation and propulsion [1]. The ablative pulsed plasma thruster (APPT) is a type of electric thruster with high

reliability, low cost, a specific impulse of around 1000 s, and a compact system [2–4]. These advantages make APPTs suitable for small satellites such as CubeSats and nano-satellites [5, 6]. It is well known that the APPT was the first EP device to be implemented on a spacecraft in orbit (Zond 2) [7, 8]. However, its main drawback of a low efficiency has resulted in its comparative under-utilization. Recently, our group proposed an asymmetric segmented anode APPT that was shown to improve the impulse bit and the thrust efficiency by up to 28% and 49%, respectively, when compared with conventional symmetric parallel-plate electrodes [9]. These improvements can be easily applied to almost all existing APPT designs in order to improve their discharge performance. However, many of the operating mechanisms and plasma processes behind the segmented anode APPT still remain unknown.

APPTs operate in a pulsed mode and typically use solid polytetrafluoroethylene (PTFE) as a propellant, but other alternatives such as liquid and gaseous propellants have also been investigated [10–14]. The main thrust production process of an APPT can be divided into ablation, ionization, and acceleration. It can be described as a spark plug triggering the main discharge and the main discharge arc ablating the PTFE propellant while ionization also takes place on the propellant surface. Then, self-induced electromagnetic forces accelerate the plasma and produce thrust. However, these processes occur in $\sim$10 μs and encompass several physical phenomena such as ionization [15], ablation [16], plasma acceleration [17], and plasma propagation [18]. Unlike single-component plasma thrusters such as ion and Hall thrusters [19, 20], APPT plasmas have a complex composition with multiple species (C, C^+, F, F^+, C_2, CF, CF_2, etc). Thus, the physical mechanisms and interactions that occur inside the APPT discharge channel (the volume between the electrodes) are very challenging to study.

Different areas regarding the APPT's low performance have been studied by many researchers. The effect of the propellant and electrodes on the APPT's performance has been studied by several researchers [21–24]. The shape and angle of the electrodes with respect to their impact on the efficiency has also been studied by Schönherr *et al* [25]. Antonsen *et al* proposed that the PTFE propellant continues to be ablated even after the termination of the discharge, resulting in a decrease in the propellant utilization efficiency, a phenomenon now called late-time-ablation (LTA) [26]. In addition to LTA, a secondary discharge has also been observed in many capacitive discharges and is referred to as 'restrikes' [27]. The restrike phenomenon has been identified to be a problem that wastes the capacitor energy in follow-up discharges after the first main discharge cycle [17]. With the asymmetric segmented anode schematic, although it significantly improved the experimental APPT's performance [9], the physical mechanisms responsible still remain unknown. To resolve this, it is necessary to understand the plasma distribution and behavior of associated neutral particles when a segmented anode is used with an APPT.

In this work, the physical mechanisms and plasma propagation process of a recently reported segmented anode APPT [9] were studied. We aim to demonstrate the physical
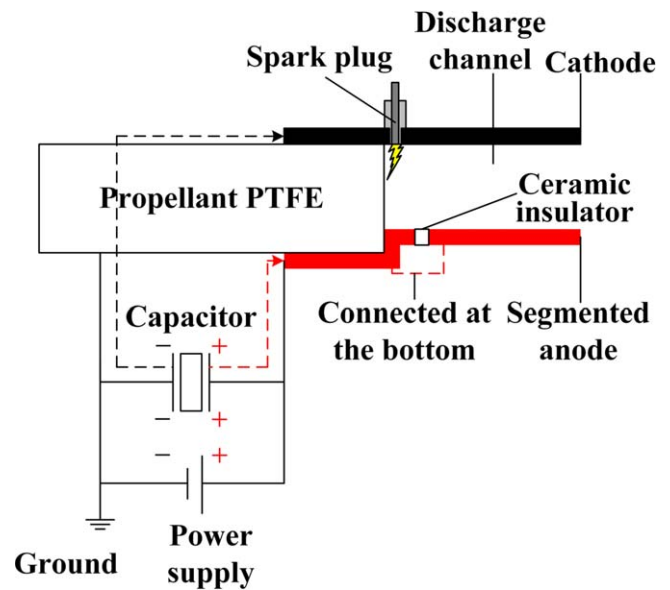

Figure 1. Segmented anode APPT schematic.

processes of a segmented anode 20 J APPT with a rectangular geometry. To gain a deeper understanding of the performance improvement associated with a segmented anode, high-speed camera imagery combined with optical filters, magnetic probe data, and long-duration imagery were obtained. An APPT with different types of anode configurations (a continuous normal anode and a segmented anode with its length asymmetric with the cathode) were studied, with a focus on the differences in the plasma morphology, arc luminosity, and plasma propagation processes.

2. Experimental facilities and methods

2.1. Segmented anode APPT and vacuum system

The APPT used in this experiment has a breech-fed PTFE schematic and a 10 μF oil capacitor. The studied discharge energies ranged from 2.5 $\sim$ 20 J. A typical discharge current curve exhibited a damped sinusoidal ring-down with a 5 μs/cycle and discharge completion in 10 μs. Discharge currents I were measured using a Rogowski coil positioned along the anode-side of the APPT circuit and discharge voltages V were measured using a Tektronix P5100A outside the vacuum chamber in parallel with the power supply circuit [28]. A segmented anode was made from copper with the upstream and downstream segments insulated from each other using a ceramic segment (machinable fluorophlogopite-based glass ceramic). At the same time, the upstream and downstream segments were electrically connected at the bottom as shown in figure 1 (not to scale). The electrical connection should also be able to maintain a downstream electric field between the electrodes while the ceramic segments may enhance the discharge arc's current density [9]. The electrode length was 15 mm for a normal APPT layout; for the segmented anode layout, there was a ceramic segment (2 mm in length) located 4 mm from the propellant surface, followed by
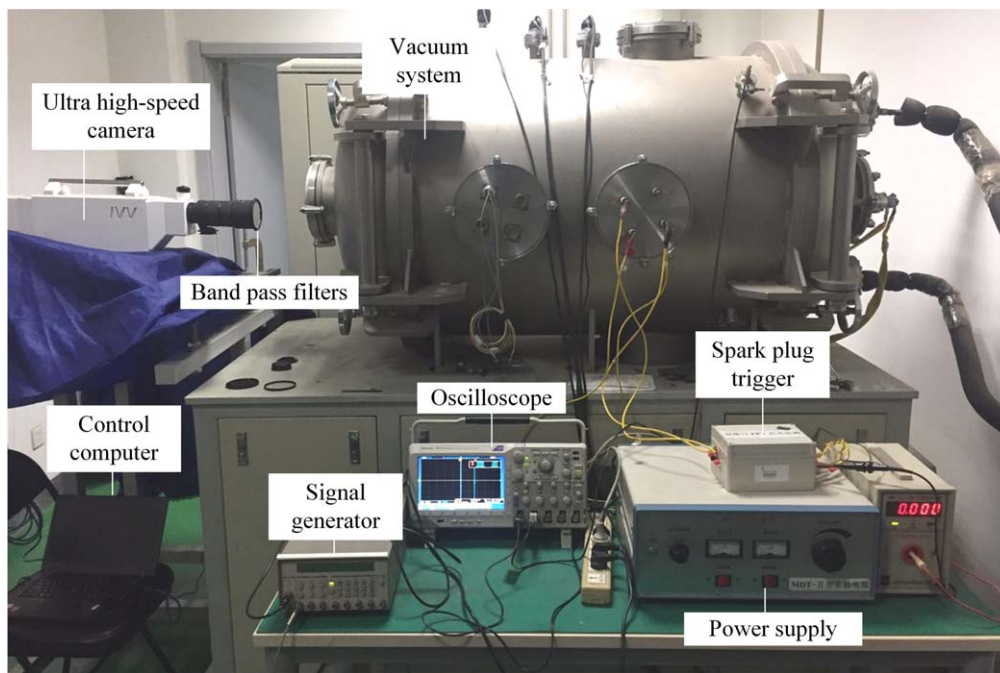
Figure 2. Photograph of the high-speed imaging system.
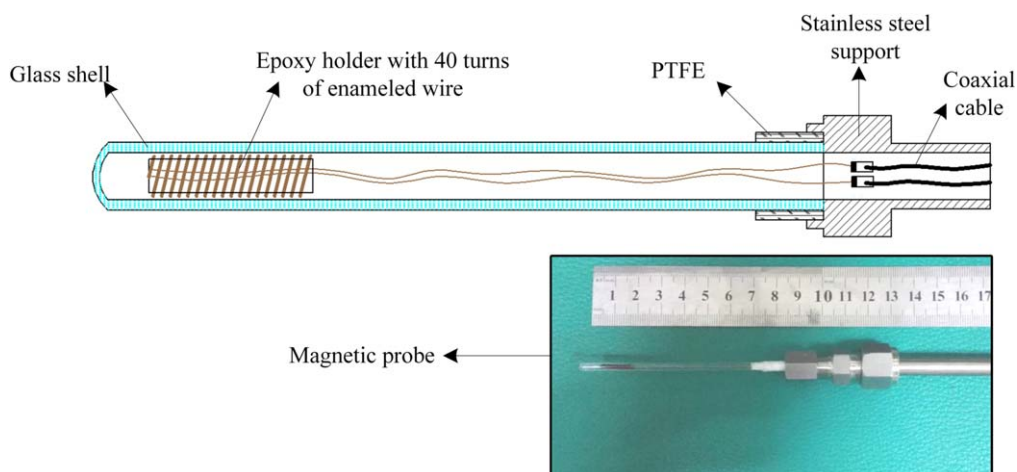

Figure 3. Magnetic probe schematic. The inset shows a photograph of the probe.

a downstream segment that brought the total length to 15 mm. The gap between the anode and cathode was 20 mm and the electrode width was 18 mm. The properties of the ceramic and images of the segmented anode APPT are provided in the supporting material, which is available online at stacks.iop. org/PSST/28/025008/mmedia.

The APPT experiments were carried out in a vacuum chamber with a diameter of 0.8 m and a length of 1.8 m. The chamber was equipped with a DIS-500 rotary pump and a CRYO-U 12HSP cryogenic pump. The base pressure was less than 3×10^{-3} Pa before the experiments.

2.2. Ultra-high-speed camera and optical filters

The APPT operating mechanism was studied through the arc morphology, plasma propagation, and restrike phenomenon using an ultra-high-speed camera (Invisible Vision, Ultra UHSi 24) with a Nikon AF-S 70-200 mm f/2.8E lens. This is a high-speed framing camera with a 16 megapixel GigE-linked CCD that can take a series of 24 images at a maximum frame rate of 200 million frames per second (fps). In our experiments, images were taken at a frame rate of 1–10 million fps with an exposure time of 100 ns and a gain of 100. Twelve images were taken in one APPT firing. The delay between each high-speed image was 0.6 μs with a total capture time of 7.2 μs, meaning that the 12 successive images were taken during the first to third half-cycle of the APPT operating process in one discharge. In the first to third half-cycle, phenomena such as restrikes, plasma propagation, and plasma acceleration have already taken effect. Furthermore, based on our discharge voltage and current data, most of the energy ($\sim$73%) is consumed in these stages. Two
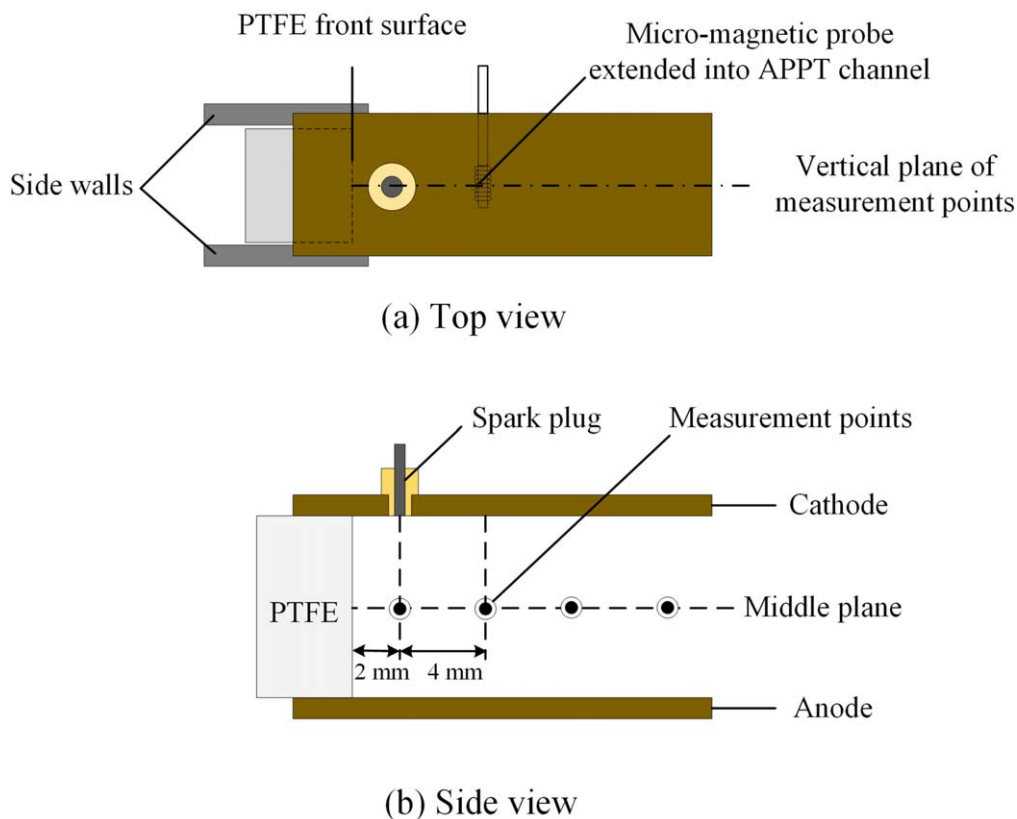
Figure 4. Micro-magnetic probe measurement points.

wavelengths were selected for imaging in addition to broadband light emission: 514.5 nm emission from neutral C_2 and 426.8 nm emission from C^+ ions [17]. An arc discharge is the electrical breakdown of a gas that produces an ongoing electrical discharge. During the operating process of all APPTs, it is the discharge arc that directly feeds the plasma. However, immediately after the onset of the discharge, due to the high energy concentration, the plasma inside the arc will contain highly ionized ions such as C^{3+} and possibly even C^{4+} ions. Due to the extreme dynamic temporal and spatial changes in the ion composition of the discharge arc, when identifying the arc, it is more accurate to refer to the neutral particles that result in the production of all the different ion species. Therefore, neutral C_2 emission was used to identify the discharge arc morphology. Narrow bandpass filters with a diameter of 70 mm (Shenzhen Nano Macro Photoelectric Technology Co., Ltd) were used to isolate the relevant emission wavelengths. These bandpass filters could be used to observe single-component behavior of the plasma. The filters have central wavelengths of 514.5 ± 2 nm and 426.8 ± 2 nm and a full-width-half-maximum of 10 ± 2 nm.

Long-duration images with these filters were also captured using a commercial Nikon D750 camera with the same lens as used on the ultra-high-speed camera. The commercial camera has the advantage of a high spatial resolution, much higher than the CCD output of high-speed cameras, and is also easily available. In the long-duration mode, all light emissions from the APPT were captured with an exposure time (2 s) far greater than the discharge time of ~ 10 μs; this presents a composite of the entire discharge process in a single image. As the exposure time is far greater than the discharge time, accurate shutter timing is not required as long as the shutter is open during the discharge. Additional filter information including wavelength curves are provided in the supporting material.

The entire high-speed imaging system consisted of an ultra-high-speed camera (Ultra UHSi 24), a signal generator (SRS DG535), an oscilloscope (Tek DPO3014), a high-voltage probe (Tek P5100) to detect the spark plug trigger, a high-voltage probe (Tek P5100A) to detect the APPT discharge voltage, a Rogowski coil, and a control computer. A photo of the high-speed image system is shown in figure 2. For all APPTs, there is an inherent delay between the spark plug firing and the onset of the discharge [29, 30]. The spark plug was used as the trigger to input a signal into the signal generator. The signal generator outputs a standard TTL signal into both the oscilloscope and high-speed camera; the spark plug signal and the high-speed camera input signal were isolated from each other. The camera's control software was used to change the camera's shutter delay to coincide with the onset of the APPT discharge (based on the Rogowski coil's current curve). Finally, we can measure the discharge voltage and current, spark plug signal, and shutter timing of the TTL signal simultaneously in one discharge using the oscilloscope.
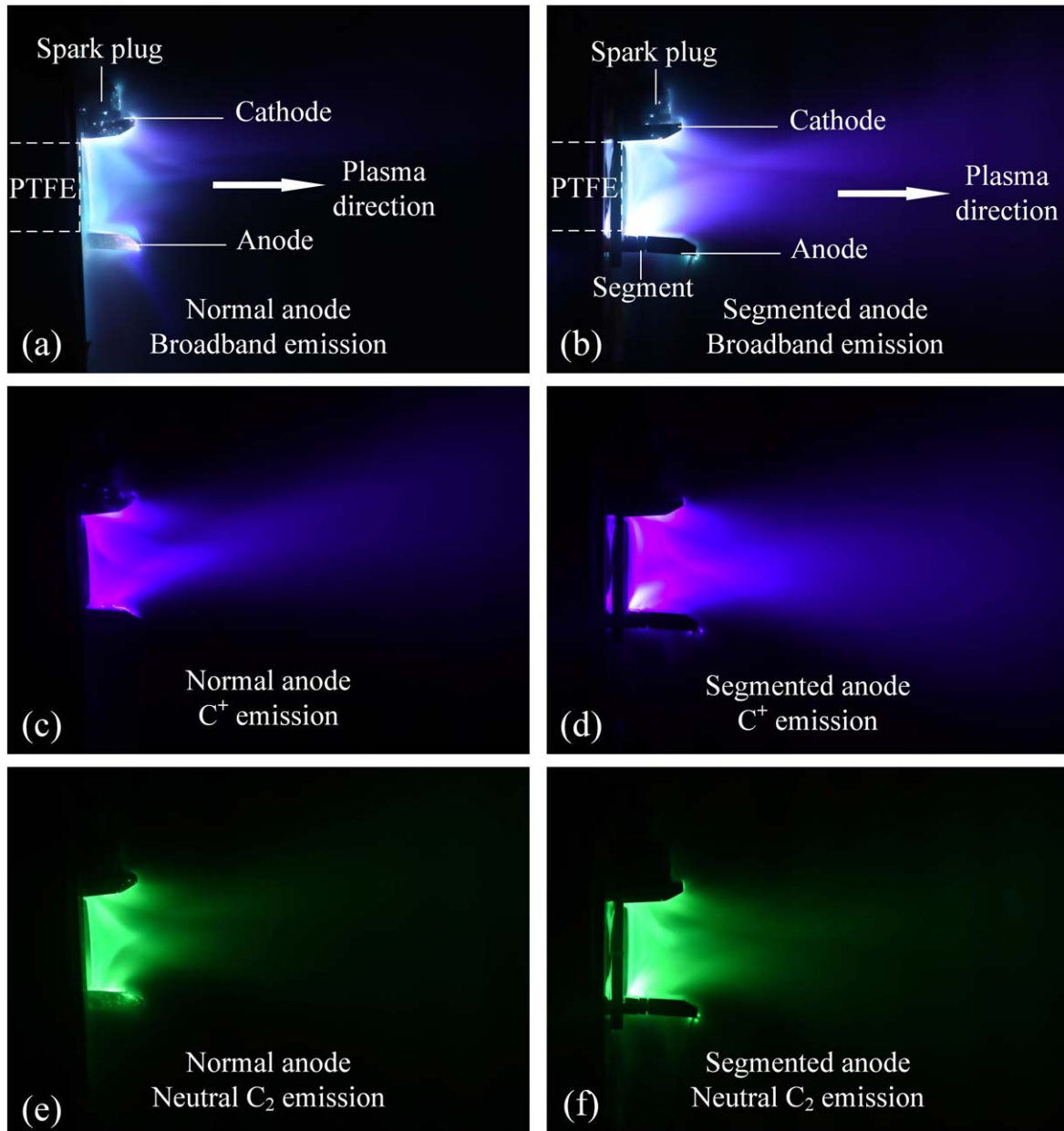
Figure 5. Side-view long-duration exposure images of the discharge morphology for APPTs with a (a) normal anode with broadband emission, (b) segmented anode with broadband emission, (c) normal anode with C^+ emission, (d) segmented anode with C^+ emission, (e) normal anode with neutral C_2 emission, and (f) segmented anode with neutral C_2 emission.

2.3. Magnetic probe

A micro-magnetic probe developed by our group was used in this experiment to determine the magnetic field variation inside the discharge channel (the space between the anode and cathode) during the APPT working process. A schematic as well as a photograph of this magnetic probe can be seen in figure 3. Since the probe needed to be extended between the electrodes to detect the magnetic field strength, it needed to be small and well-shielded against the discharge noise and high temperature. The entire diameter of this micro-magnetic probe is less than 3 mm. There were 40 turns of enameled wire wound on an epoxy resin core holder with a diameter of 2.5 mm; the exterior was covered with a glass shell.

The measurement points are shown in figure 4. The micro-magnetic probe was extended between the electrodes and was located along the central vertical plane perpendicular to the front surface of the PTFE. Four measurement points were used inside the inter-electrode space along the downstream direction toward the thruster exit to obtain the magnetic field variation (for both the normal and segmented anode APPTs). The distances to the PTFE surface were 2, 6, 10, and 14 mm.

3. Experimental results

3.1. Long-duration plasma component imagery

Various long-duration images with different bandpass filters of the entire discharge process can be used as a visual aid to
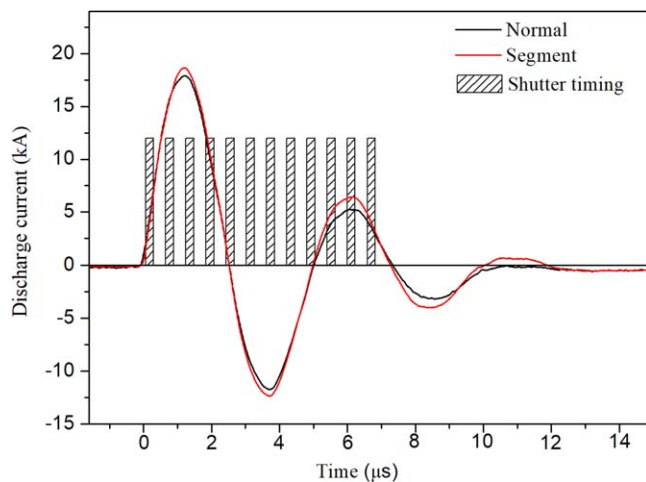
Figure 6. Discharge currents of normal and segmented anode APPTs with the ultra-high-speed camera's shutter timings.

identify the physical mechanisms of a segmented anode APPT. Both the normal and segmented anode APPTs were tested at an initial discharge voltage of 1800 V (16.2 J). Figure 5 shows side-view images of the APPT discharge for a (a) normal anode with broadband emission, (b) segmented anode with broadband emission, (c) normal anode with C^+ emission, (d) segmented anode with C^+ emission, (e) normal anode with C_2 neutral emission, and (f) segmented anode with C_2 neutral emission. The images were manually triggered with an exposure time (2 s) far greater than the discharge time of ~10 μs (any error due to manual triggering does not affect the capture of all the discharge light during the camera's exposure time. A schematic of this can be found in the supporting information); this presents a composite of the entire discharge process in a single image.

There appears to be clear qualitative differences between normal and segmented anode APPTs. When comparing the broadband emissions in figures 5(a) and (b), the luminosity pattern is brighter for the segmented anode APPT than that of the normal anode APPT. The band originating from the upstream segment also never appears with the conventional normal anode APPT. The properties of this bright band will be further discussed with high-speed imagery data shortly. When comparing the C^+ emissions in figures 5(c) and (d), there is a significant bright section in the segmented anode APPT at the upstream location before the ceramic segment. When comparing the neutral C_2 emissions in figures 5(e) and (f), the brightness pattern is also seen to be focused upstream before the ceramic for the segmented anode APPT while the same brightness pattern is distributed along the entire anode for a normal anode APPT. This bright band is extremely repeatable and is present on every image taken for a segmented anode APPT. Further examples can be found in the supporting material. The bright band may occur because the segmented anode APPT's arc migration is restricted before the ceramic segment, resulting in the discharge arc at the corner being better resolved.

3.2. Discharge current and magnetic field

Figure 6 shows typical discharge current curves and the shutter timings of the ultra-high-speed camera for normal and segmented anode APPTs with an initial discharge voltage of 1800 V (16.2 J). These current waveforms had good reproducibility and the curves in figure 6 are the averaged data over 50 discharges. The error between the shutter capturing the first image and the onset of the discharge current is typically less than 0.1 μs.

When the segmented anode is compared to a normal anode, there is a change of less than 6% in the peak values of the discharge currents. The repeatability error (shot-to-shot error) for the normal anode is 2.7% when compared to the average value. This shows that the normal and segmented anode APPTs have similar discharge current characteristics during the first peak. However, the restrikes have apparent peak differences (the segmented anode's third peak is 24% higher than that of a normal anode APPT). This may be due to the different plasma density and restrike position inside the different types of discharge channels.

The magnetic probe was extended into the inter-electrode area of the APPT to carry out measurements. The magnetic field histories for 1800 V discharges (16.2 J) with a normal and segmented anode are shown in figure 7. Each curve was averaged from five shots and the distances to the PTFE surface are labeled using different lines. Since the generated plasma may be randomly distributed within the discharge area during each APPT discharge, the standard deviation was relatively high at approximately 20%. However, the phase error of separate shots was less than 0.1 μs; this indicates that the plasma propagation process was stable.

The inter-electrode magnetic field strength is related to the distribution of the discharge current in the discharge channel, and the spatial variations of the magnetic field indicate the acting position of the electromagnetic force. There is a clear peak delay between upstream and downstream measurement points. This signal delay corresponds to the delay in the arrival of the plasma in the current sheet driven by the main discharge of the APPT. Using the time difference between the signal peaks and the measurement point distances, the velocities of the plasma could be roughly estimated to be 23 and 19 km s^{-1} for the normal and segmented anode, respectively. The curves for the measurement points very near to the propellant surface (2 mm from the PTFE surface) have several small peaks that originate from noise during the discharge process. This may be due to spark plug noise and random plasma fluctuations. Nevertheless, the general curve is repeatable, and five repeated measurements can be found in the supporting material that demonstrate this. The estimated velocities are at similar levels (around 20 km s^{-1}), which indicates that the plasma propagation process and acceleration mechanism for the normal and segmented anode APPTs should be similar. The reason behind the improvement in the impulse bit and thrust efficiency of a segmented anode APPT should therefore focus instead on the ablation, ionization, and plasma morphology characteristics.
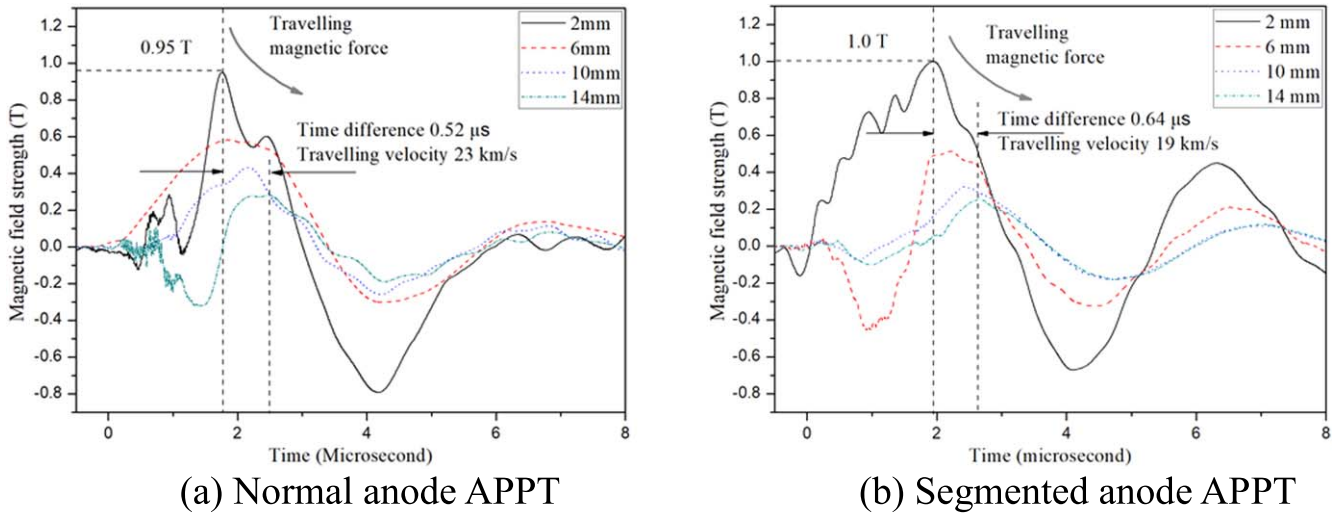
Figure 7. Normal and segmented anode APPTs' magnetic field strength with downstream distance.

3.3. Plasma propagation imagery

High-speed images for normal and segmented anode APPTs are compared in figures 8–10 Locations and geometries of the cathode, anode, ceramic segment, and PTFE are shown in these images using dotted lines. Figure 8 shows the broadband light emission (no filter) with an f-number of f/11 and a gain of 100; figure 9 shows the 426 nm emission from C^+ ions with f/5.6 and a gain of 100; figure 10 shows the 514 nm emission from neutral C_2 with f/5.6 and a gain of 100. Both the normal and segmented anode APPTs were tested at three initial voltage levels (1200, 1500, and 1800 V) and were repeated at least five times. In order to best highlight the arc morphology and APPT operating process, the figures shown correspond with an initial discharge voltage of 1800 V, which produced the highest luminosity.

From figure 8, we can clearly see two obvious differences: 1. The different discharge arc morphologies between anode types during the onset of the main discharge at 0 μs; 2. The difference in arc propagation from 2.4–6 μs. These two differences originate due to the ceramic segment of the segmented anode APPT.

For the 0 μs high-speed images, the bright electrical patterns exhibit an 'I' shape for the segmented anode while the normal anode APPT's initial arc exhibits an 'L' shape. For both the normal and segmented anode APPTs, the bright 'I' section is the initial discharge arc. However, for the normal anode, there is also electrical current passing along the surface of the anode, making the normal anode APPT's initial discharge pattern appear as an 'L'. For the segmented anode, the main discharge arc is restricted by the ceramic segment. The more diffuse distribution of a normal anode may result in a lower current density on the PTFE surface when compared with a segmented anode.

In Figure 8(b) (1.2 μs image), we defined an 'attachment point' for the discharge arc of the APPTs, which is the point where the arc attaches to the anode. The lower attachment point of the arc is restricted by the end of the upstream segment. From 2.4–6 μs, the arcs propagate downstream as time

progresses for both the normal and segmented anode APPTs. However, the segmented anode APPT's arc's attachment point stays in the same position at the end of the upstream segment (this can be seen in figure 8(b) for 2.4–6 μs) while the normal anode APPT's arc continues moving downstream. As can be seen in figure 6, the restrike period ranges from 2.7–12 μs. Therefore, the high-speed images of 4.8 and 6 μs occur during the restrike period of the APPT operating process. During the restrike period, the discharge arc of the segmented anode is also restricted nearer to the propellant surface (where it can possibly ablate more solid propellant and increase the overall level of ionization) while the discharge arc of a normal APPT travels even further downstream. From the qualitative plasma morphology, the segmented anode schematic clearly better optimizes the main discharge arc position and the restrike process when compared with a conventional symmetric parallel-plate APPT.

The C^+ emission images in figure 9 show apparent differences in the ablation, ionization, and restrike processes between the normal and segmented anode APPTs. For the main discharge process (0–2.4 μs), C^+ light emission from the segmented anode APPT is much higher than that from the normal anode APPT. This indicates that the segmented anode APPT exhibits greater ionization than the normal anode APPT during the main discharge process. This is also supported by the magnetic probe and Langmuir probe data in [9]. For the follow-up discharge cycles (3.6–6 μs), the C^+ plasma morphology and density are significantly different. The triangular shape of the segmented anode APPT's plasmoid matches up with the restricted downstream arc in figure 8. This is consistent with the result from [17] that the restrike plasma originates from the leading edge of the discharge arc. Highly visible C^+ emission was observed from the leading edge of the discharge arc at the upstream section of the segmented anode APPT (figure 9(b) 3.6–6 μs), while only weak C^+ emission was observed from the normal APPT (figure 9(a) 3.6 μs). This suggests that the restricted discharge arc affects the ionization process in the follow-up restrike cycles of a segmented anode APPT's discharge.
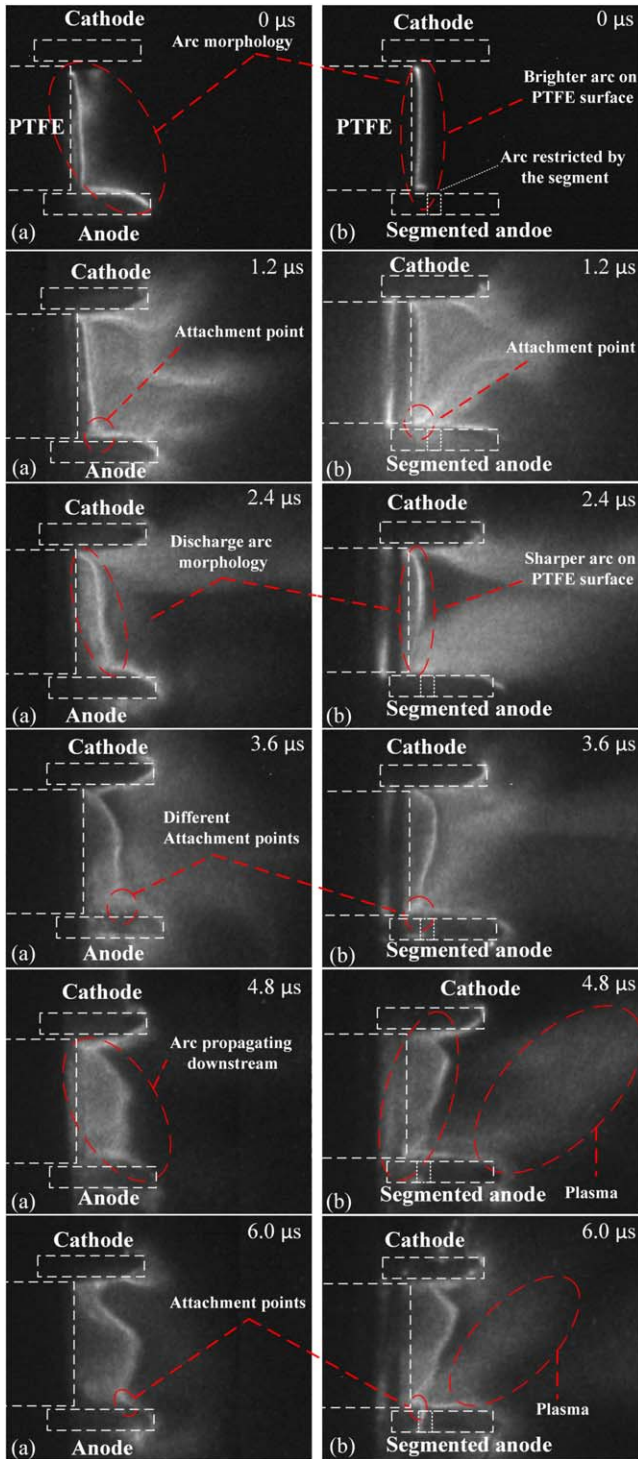
Figure 8. Side-view of the plasma morphology f (a) a normal and (b) segmented anode APPT using broadband emission high-speed images. A frame rate of 1.667 million fps, f/11, exposure time of 100 ns, and a CCD gain of 100 was used. The APPT's initial discharge voltage was 1800 V (16.2 J).
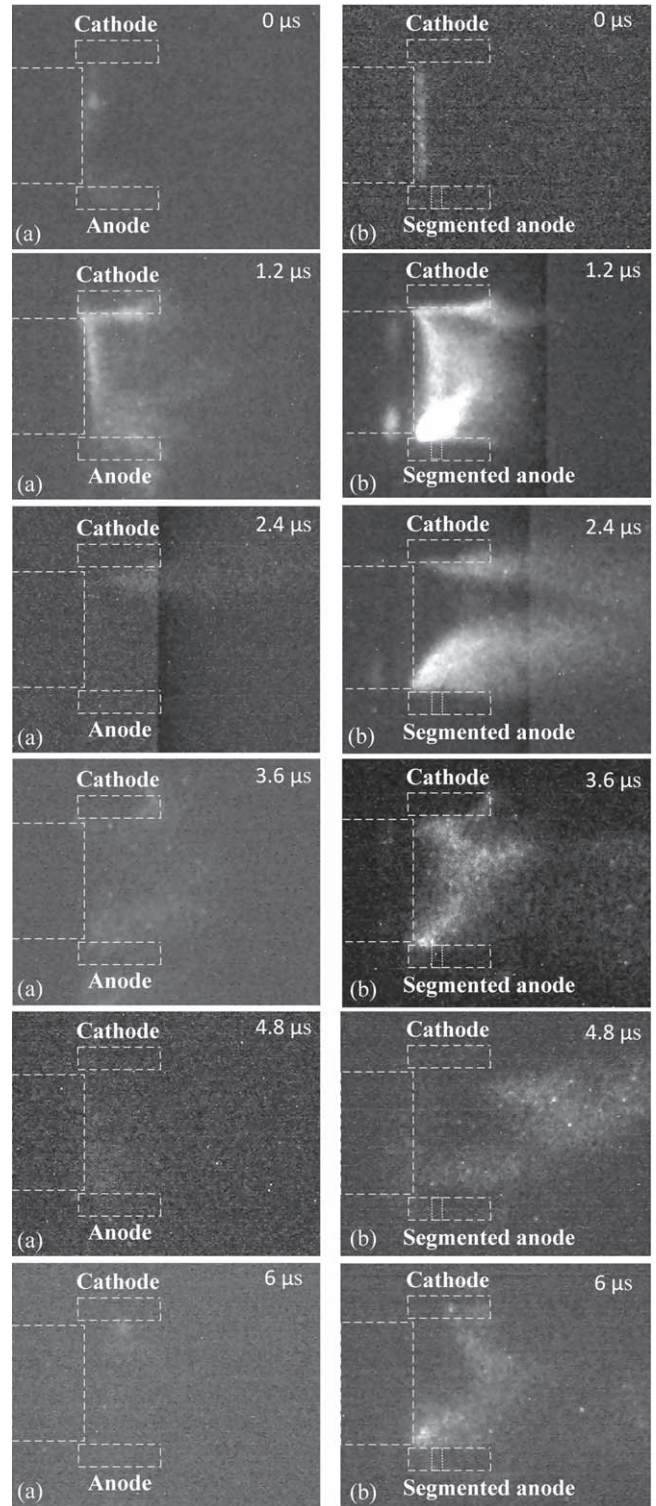

Figure 9. Side-view of the plasma morphology of (a) a normal and (b) segmented anode APPT using C^+ emission high-speed images observed with a 426 nm narrowband filter. A frame rate of 1.667 million fps, f/5.6, exposure time of 100 ns, and a CCD gain of 100 was used. The APPT's initial discharge voltage was 1800 V (16.2 J).

Figure 10 shows the neutral C_2 emission using the 514 nm narrowband filter and can be used to identify the discharge arc morphology. During the main discharge period (0–2.4 μs), the arc morphology of the segmented anode APPT is similar to that of the normal anode APPT. However, during

the arc propagation process (3.6–6 μs), the arc morphology of the segmented anode APPT deviates significantly from the normal anode APPT. Due to thermal expansion, the arc moves downstream after the main discharge period; this can
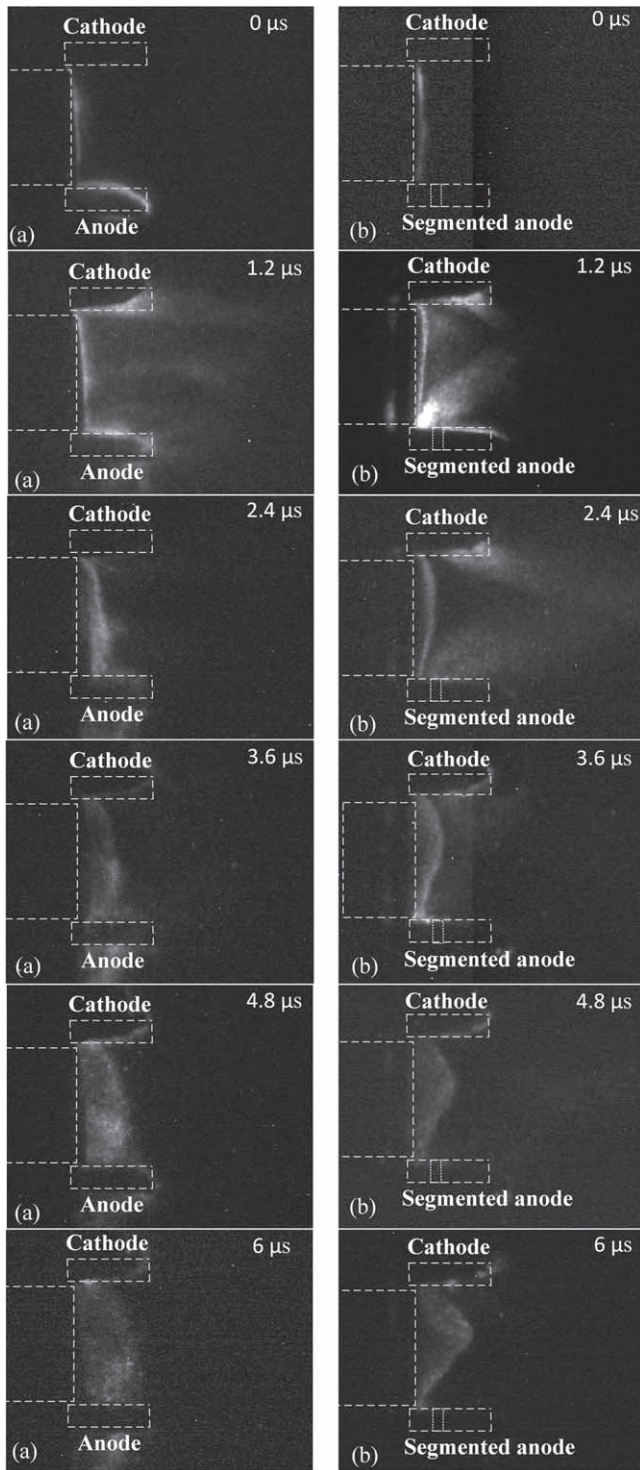
Figure 10. Side-view of the plasma morphology of (a) a normal and (b) segmented anode APPT using neutral C_2 emission high-speed images observed with a 514 nm narrowband filter. A frame rate of 1.667 million fps, f/5.6, exposure time 100 ns, and a CCD gain of 100 was used. The APPT's initial discharge voltage was 1800 V (16.2 J).
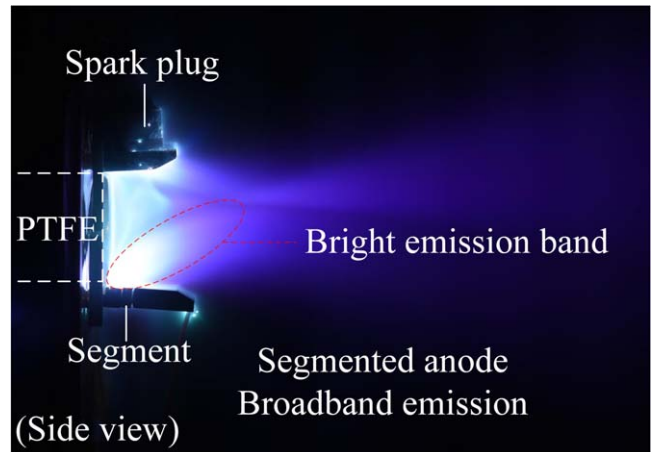

Figure 11. Side-view of the bright band originating from the upstream segment in a segmented anode APPT. Initial discharge voltage of 1800 V (16.2 J).

normal anode APPT continually travels downstream along the anode. A stable upstream attachment point on the anode will restrict the arc nearer to the propellant surface. This may promote ionization and stabilize the discharge arc morphology.

4. Discussion

4.1. High frame rate analysis for segmented anode APPT

It is interesting to note that there is a bright band originating from the upstream segment in the broadband long-duration images in figure 11, which never appears in a conventional normal anode APPT. In our previous work, the origin of this band was unclear [9]. However, with the narrow bandpass filters and high-speed camera data, it is possible to analyze the components and characteristics of this bright band. Figure 12 shows 10 million fps comparisons of C^+ and C_2 emission for a segmented anode APPT with an initial discharge voltage of 1800 V (each image has a time difference of 0.1 μs, shorter than the previously shown images; this time difference was chosen to cover the main discharge period).

Figure 12 shows the initial development of C^+ and neutral C_2 during the main discharge period of a segmented anode APPT. For the C^+ emission, the initial 0.1–0.3 μs period is an increasing ionization process, while from 0.5–1.1 μs, the bright ionization point on the anode corner became stable. For the neutral C_2, the entire process from 0.1–1.1 μs shows a band originating at the anode corner before the upstream ceramic and develops into a large area with a high brightness band. From [17], the neutral particle velocity is in the range of $\sim$1 km s^{-1}. However, the band in figure 12(b) moves far faster than the neutral particle velocity. We presume that this C_2 band originates from collisions in the dense plasma plume.

From the data, we can obtain a general understanding of the main discharge process of a segmented anode APPT. The main ionization area of the segmented anode APPT is near the
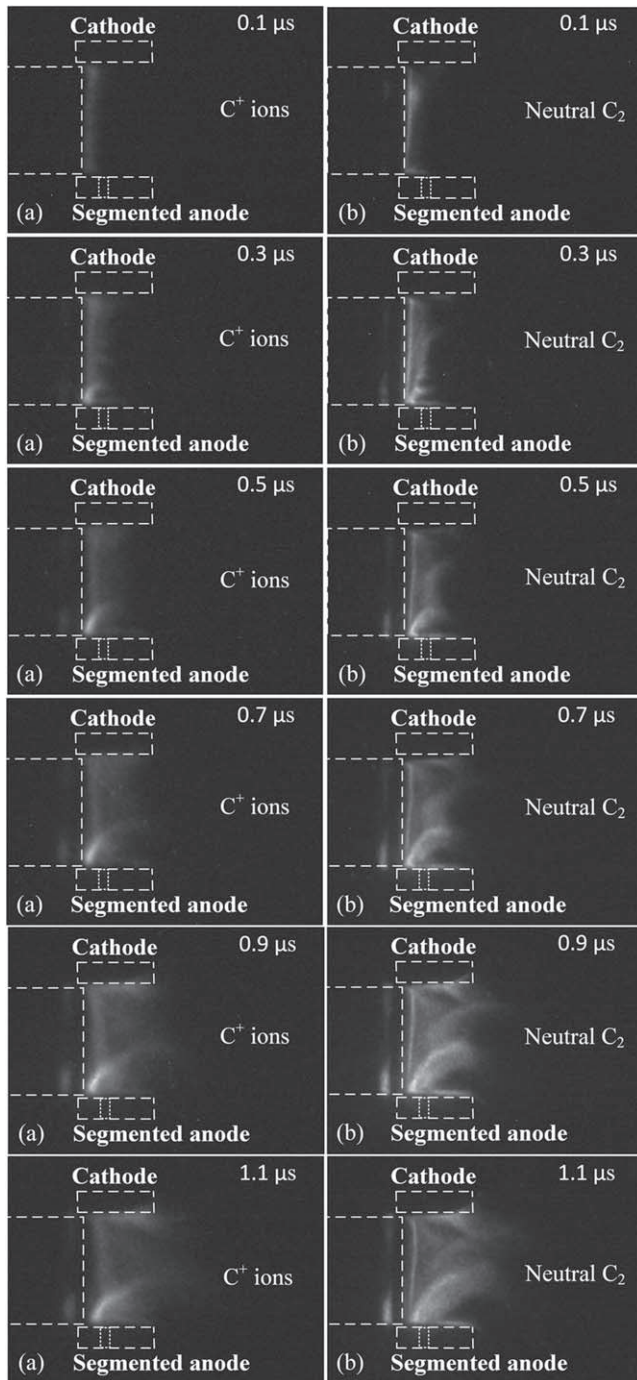
be called downstream arc migration. However, differences appear in the attachment points depending on the anode type. The segmented anode APPT's arc migration is restricted by the ceramic segment. However, the attachment point of the

Figure 12. Side-view high-speed images of a segmented anode APPT with (a) C^+ emission (426 nm filter) and (b) neutral C_2 emission (514 nm filter). A frame rate of 10 million fps, f/5.6, exposure time of 100 ns, and a CCD gain of 100 was used. The APPT's initial discharge voltage was 1800 V (16.2 J).

PTFE surface at the anode corner. Since the arc is restricted, the ionization area and position is quite stable during the main discharge process. This results in a plasma density near the anode corner that is higher than that of a normal anode APPT. Thus, a visualized bright band appears during the segmented anode APPT discharge process. The neutral C_2 light emission from this band further suggests that significant collisions occur within the plasma.

4.2. Relationship between restrike images and thrust data

It is acknowledged that the restrike is an unavoidable phenomenon that occurs in the follow-up discharge after an APPT's main discharge period [17]. However, the segmented anode APPT shows clear arc morphology and plasma morphology differences when compared with a normal anode APPT. Figure 13 shows high-speed image comparisons for normal and segmented anode APPTs with C_2 emission and C^+ emission filters. The time range was chosen to be the current reversal period during the secondary discharge cycle at 3 μs. The initial discharge voltage was 1800 V.

Figure 13 is a comparison of the restrike position of the arc and the ionization position of C^+ emission between normal and segmented anode APPTs. The top row shows 514 nm emission (neutral particles and the discharge arc) and the lower images show 426 nm emission (C^+). The red dotted line indicates the approximate leading edge of the restrike position. The restrike plasma originates from the leading edge of the arc as shown by the red dotted line. At 3 μs, the discharge arc of the segmented anode APPT is restricted by the upstream ceramic segment. Thus, the plasma's formation position for the segmented APPT is also nearer to the propellant surface. The magnetic probe data showed that the plasma velocity inside the segment anode APPT is lower than that of a continuous electrode APPT; this is consistent with the plasma morphology lag in figures 13(c) and (d). At 3.6 μs, the brightness patterns for C^+ emissions show apparent differences. The attachment point at the segmented anode corner before the upstream segment emits stronger C^+ emissions than that of a normal anode APPT. The restrike was restricted to the upstream location (the anode corner before ceramic segment), which may make it possible for this discharge arc to better ionize the propellant in restrikes.

If the segmented anode can result in a larger proportion of the restrike energy being used in ablation and ionization, this will be reflected in impulse bit data. The impulse bit of a segmented anode APPT and a normal APPT is shown in figure 14 (the impulse bit measurement system was developed by our group and information can be found in [9]). The energy ranges from 2.5–20 J and 10 points were chosen to show the impulse bit relationship of a segmented anode APPT. Seven points were chosen to show the impulse bit relationship of a normal anode APPT. Every data point has data from five shots to ensure repeatability.

In figure 14, there appears to be a slope difference (13.5 versus 14.8 μNs J^{-1}) above and below an energy level of approximately 8.5 J for the segmented anode APPT. The standard errors for these slopes are in the order of 0.4 μNs J^{-1}. Conversely, the slopes above and below approximately 8.5 J for the normal APPT are 11.5 and 11.8 μNs J^{-1}, with standard errors in the order of 0.71 and 0.32 μNs J^{-1}, respectively. We can hypothesize the different slope for a segmented anode APPT may be because at energy levels of less than approximately 8.5 J for our APPT, the restrike energy is not high enough to significantly ionize neutral particles for either the normal or the segmented anode APPT. When the energy is higher than 8.5 J, the segmented anode APPT's restrike energy may begin to better ionize the propellant in the follow-up discharges. It may be
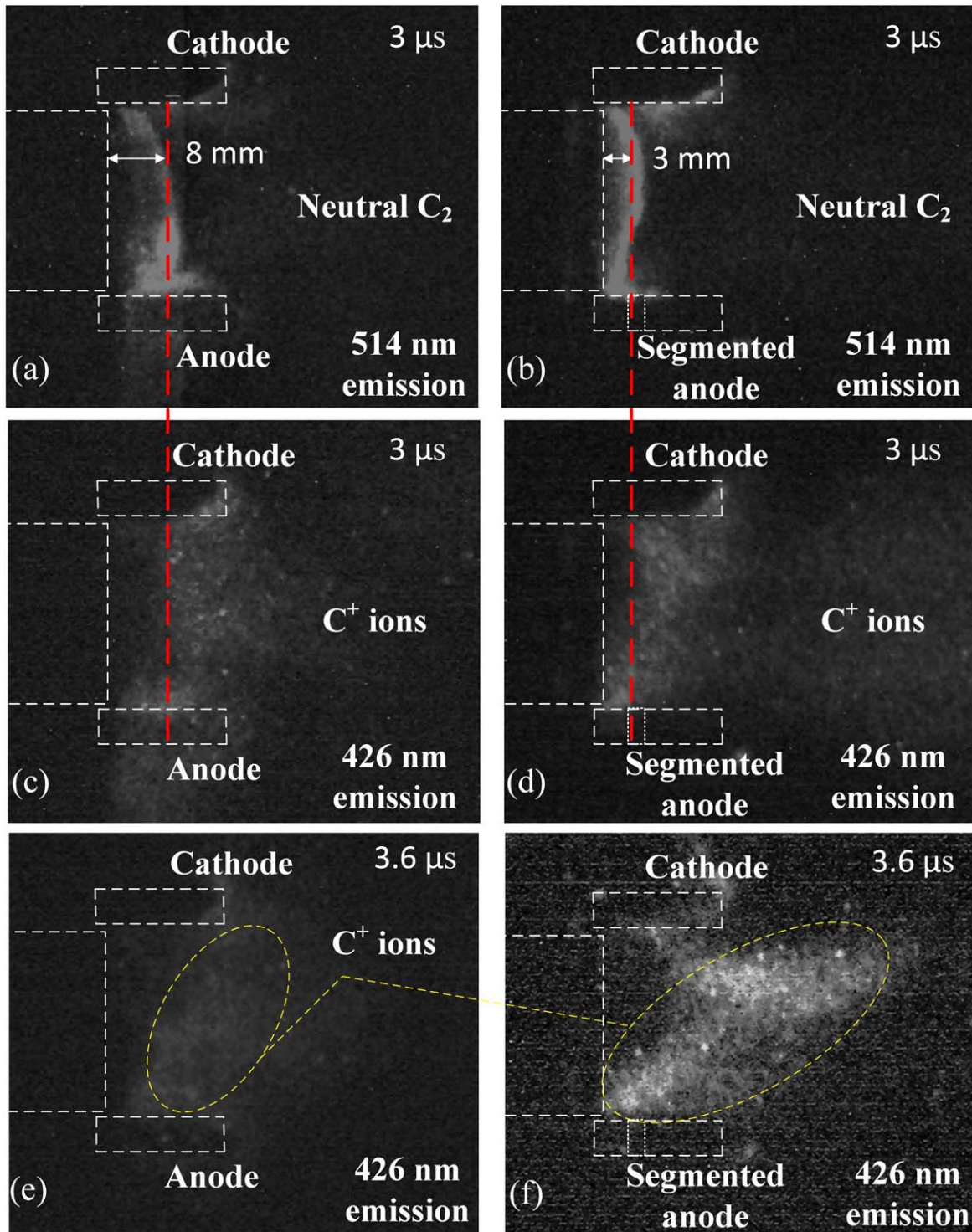
Figure 13. Side-view high-speed images of a normal and segmented anode APPT with (a), (b) neutral C_2 emission (514 nm filter) and (c)–(f) C^+ emission (426 nm filter). A frame rate of 1.667 million fps, f/5.6, exposure time 100 ns, and a CCD gain of 100 was used. The APPT's initial discharge voltage was 1800 V (16.2 J).

possible that even more significant differences will appear at even higher energy levels.

4.3. General applicability of a segmented anode

We showed here that the use of a segmented anode results in a change in the fundamental physical process of APPT

operation. When a continuous anode is used, it is common behavior that APPTs will all exhibit the same physical process of a discharge arc traveling downstream after ablation of the propellant. This has been demonstrated in previous publications, including for optimized APPTs such as the ADD SIMP-LEX [18] and Japan's APPT [17]. This inherent physical process of the discharge arc traveling further away from
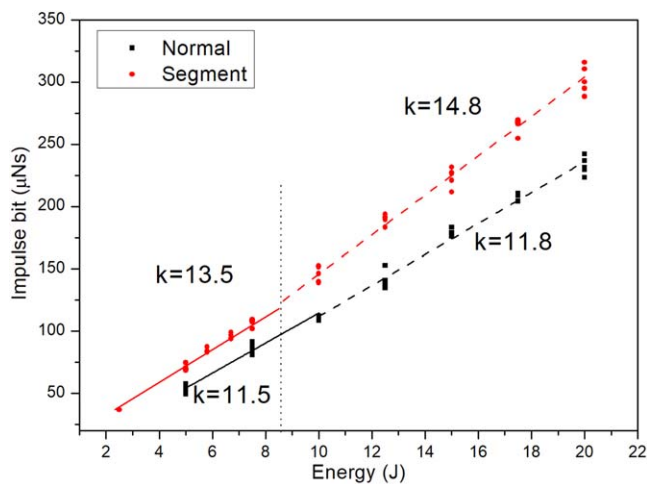
Figure 14. Impulse bit measurements for the normal and segmented anode APPT.

the propellant surface over time will limit ablation, ionization, and acceleration close to the surface. While the experimental thruster here is not optimized for overall performance, we showed that the use of a segmented anode can fundamentally alter the common phenomenon of the discharge arc traveling downstream. The data also suggests that this is likely to be the reason behind the improved performance demonstrated previously with a segmented anode. As the discharge arc phenomenon is common to APPTs, this fundamental improvement should also be applicable to other APPT designs. In the future, it can also be taken as an additional new step in the overall optimization of an APPT design.

5. Conclusion

In the present work, we investigated the plasma morphology and discharge arc morphology of an asymmetric segmented anode APPT. A high-speed camera, micro-magnetic probe, and narrow bandpass filters were used to identify the details of the segmented anode APPT's operating mechanisms. The micro-magnetic probe shows that the inter-electrode plasma propagation velocity is approximately $19\,\mathrm{km\,s^{-1}}$, which is lower than that of a normal APPT at $23\,\mathrm{km\,s^{-1}}$. However, the two velocities are in the same range, which suggests a similar plasma propagation process and acceleration mechanism. Broadband high-speed images reveal that the segmented anode APPT has a bright pattern that appears as an 'I' shape, which indicates a higher current density in the initial discharge arc compared to a normal anode APPT. Filters for 426 and 514 nm emission light with high-speed images show that there are clear differences in the C^+ distribution and discharge arc morphology between a normal and segmented anode APPT. The segmented anode APPT was found to restrict the arc at the upstream segment before the ceramic segment. Thus, during the entire discharge process, the segmented anode APPT has a stable discharge arc 'attachment point' on the anode corner near the PTFE surface, which may result in greater propellant mass ablation and ionization. The

C^+ emission of a segmented anode APPT was found to be stronger and has a formation position nearer to the anode corner.

We believe that this improvement can be easily applied to almost all existing APPT designs in order to improve their discharge performance. While this paper gives us a deeper understanding of the physical mechanisms behind this asymmetric electrode APPT, further quantitative data such as the ionization rate, the effect of the upstream and downstream segment lengths, and various component densities are needed. These will possibly aid in more advanced optimization of this asymmetric electrode structure.

ORCID iDs

William Yeong Liang Ling ⓘ https://orcid.org/0000-0003-4181-1291
Haibin Tang ⓘ https://orcid.org/0000-0002-9190-7323

References

[1] Mazouffre S 2016 *Plasma Sources Sci. Technol.* **25** 033002
[2] Popov G A and Antropov N N 2007 *Development of next generation APPT at RIAME, 30th International Electric Propulsion Conferenc* (*IEPC-2007-134*) (Florence, Italy)
[3] Kazeev M N, Kozubskiy K N and Popov G A 2009 *Victor Khrabrov - pioneer of the first space electric propulsion system development and space tests 1st International Electric Propulsion Conference* (*IEPC-2009-235*) (Ann Arbor, MI)
[4] Alexeev Y A and Kazeev M N 1999 *Performance study of high power ablative pulsed plasma thruster 26th International Electric Propulsion Conference* (*IEPC-99-207*) (Kitakyushu, Japan)
[5] Levchenko I *et al* 2018 Space micropropulsion systems for cubesats and small satellites: from proximate targets to furthermost frontiers *Appl. Phys. Rev.* 011104
[6] Panetta P V, Culver H, Gagosian J, Johnson M, Kellogg J, Mangus D, Michalek T, Sank V and Tompkins S 1998 NASA-GSFC nano-satellite technology development *Small Satellite Conf.* SSC98-VI-5
[7] Burton R L and Turchi P J 1998 *J. Propul. Power* **14** 716–35
[8] Schönherr T 2016 *Encyclopedia of Plasma Technology* ed J Shohet (New York: Taylor & Francis) vol 2, 1452–61
[9] Zhang Z, Ren J X, Tang H B, Ling W Y L and York T M 2018 An ablative pulsed plasma thruster with a segmented anode *Plasma Sources Sci. Technol.* **27** 015004
[10] Ziemer J, Cubbin E and Choueiri E 2013 Performance characterization of a high efficiency gas-fed pulsed plasma thruster *Joint Propulsion Conf. and Exhibit*
[11] Ling W Y L, Schönherr T and Koizumi H 2017 *J. Appl. Phys.* **121** 073301
[12] Ling W Y L, Schönherr T and Koizumi H 2017 *Appl. Phys. Lett.* **111** 014101

[13] Rezaeiha A and Schönherr T 2014 *J. Propul. Power* **30** 253–64
[14] Berkery J W and Choueiri E Y 2006 *Plasma Sources Sci. Technol.* **15** 64–71
[15] Schönherr T, Nees F, Arakawa Y, Komurasaki K and Herdrich G 2013 *Phys. Plasmas* **20** 033503 (1-8)
[16] Yang L, Liu X, Wu Z and Wang N F 2014 *Appl. Phys. Lett.* **104** 084102–4
[17] Koizumi H, Noji R, Komurasaki K and Arakawa Y 2007 Plasma acceleration processes in an ablative pulsed plasma thruster *Phys. Plasmas* **14** 033506–10
[18] Schönherr T, Komurasaki K and Herdrich G 2011 Study on plasma creation and propagation in a pulsed magnetoplasmadynamic thruster *World Academy of Science Engineering and Technology* **50** 557–63
[19] Dan M G and Katz I 2008 *JPL Space Science and Technology Series* (Hoboken, NJ: Wiley & Sons)
[20] Zhang Z, Tang H B, Zhang Z and Cao S 2016 A retarding potential analyzer design for keV-level ion thruster beams *Rev. Sci. Instrum.* **87** 123510
[21] Palumbo D J and Guman W J 1976 *J. Spacecraft Rockets* **13** 896467–896467
[22] Rezaeiha A and Schönherr T 2012 Analysis of effective parameters on ablative PPT performance *Aircr. Eng. Aerosp. Technol.* **84** 231–43
[23] Pottinger S J, Krejci D and Scharlemann C A 2011 Pulsed plasma thruster performance for miniaturised electrode configurations and low energy operation *Acta Astronaut.* **68** 1996–2004
[24] Coletti M, Marques R I and Gabriel S B 2009 *Design of a two-stage PPT for cubesat application 31st International Electric Propulsion Conference (IEPC-2009-244) (Ann Arbor, MI)*
[25] Schönherr T, Nawaz A, Herdrich G, Röser H P and Kurtz M A 2009 Influence of electrode shape on performance of pulsed magnetoplasmadynamic thruster *J. Propul. Power* **25** 380–6
[26] Antonsen E L, Burton R L, Reed G A and Spanjers G G 2005 Effects of postpulse surface temperature on micropulsed plasma thruster operation *J. Propul. Power* **21** 877–83
[27] Lieberman M A and Lichtenberg A J 2005 *Principles of Plasma Discharges and Materials Processing* 2nd Edn (Hoboken, NJ: Wiley-Interscience)
[28] Zhang Z, Tang H, Zhang Z, Liu Q and Cao S 2015 *Non-phase-difference Rogowski coil for measuring pulsed plasma thruster discharge current 34th International Electric Propulsion Conference, (IEPC-2015-49) (Kobe, Japan)*
[29] Kamezaki H, Yano K, Kato H and Horisawa H 2018 Effect of discharge pulse delays on characteristics of a short-pulse laser-assisted pulsed plasma thruster *51st AIAA/SAE/ASEE Joint Propulsion Conf.* AIAA Propulsion and Energy Forum, AIAA 2018-4590 (Orlando)
[30] Huang T *et al* 2015 Study of breakdown in an ablative pulsed plasma thruster *Phys. Plasmas* **22** 103511